GEOPHYSICS, VOL. 68, NO. 2 (MARCH-APRIL 2003); P. 497–505, 4 FIGS.
10.1190/1.1567217

Transformation of VLF anomaly maps into apparent resistivity and phase

Michael Becken* and Laust B. Pedersen‡

ABSTRACT

We investigate a transformation of magnetic transfer functions into the tangential-electric mode part of the impedance tensor in the scope of the plane-wave electromagnetic tensor–VLF method. The transformation, which is applicable to any 2D data representing the response of arbitrary 3D geoelectric structures, overcomes the difficulties of quantitative interpretation of magnetic transfer functions, which predominantly provide a measure of the lateral changes of the electrical conductivity in the earth. We require densely sampled magnetic transfer functions of one frequency as input data. These may be decomposed into their normal and anomalous parts (deviation from the response of a layered earth) for a unit external plane-wave source field using the Hilbert transform relationship between the magnetic field components. Faraday's law then directly provides the anomalous toroidal electric field. Unfortunately, there is no chance to estimate the normal electric field from magnetic data, since the magnetic field is not sensitive to a layered earth. This constant must be provided as a boundary condition, e.g., from one ground measurement, to derive an impedance tensor and related apparent resistivities and phases.

INTRODUCTION

In Sweden, very-low-frequency (VLF) three-component magnetic data in the frequency range 14–25 kHz covering areas of several tens of thousand square kilometers have been collected by the Geological Survey of Sweden (SGU) during the last decade. By introducing the tensor-VLF concept in analogy to magnetotellurics, Pedersen et al. (1994) have derived magnetic transfer functions for each measurement point. These transfer functions (or tipper vectors) describe the linear relationship between the vertical magnetic field, which is entirely anomalous, and the horizontal magnetic field components. They are independent of source field characteristics as long as the primary field can be considered as uniform, and they only reflect lateral variations in electrical properties of the earth. Above a 1D earth (normal conductivity distribution) the tipper vector equals zero, but in 2D or 3D environments (anomalous conductivity distributions), the vector exhibits peaks around lateral (anomalous) conductivity contrasts.

The Swedish data provide in both horizontal coordinates (x, y) spatially well sampled magnetic transfer functions and are driving an investigation of the spatial relationship between magnetic field $\mathbf{H}$ and electric $\mathbf{E}$ field given by Faraday's law,

$$\nabla \times \mathbf{E} = -i\omega\mu\mathbf{H}. \tag{1}$$

Here, ω is the angular frequeny and μ is the magnetic permeability. Vallee et al. (1992) and Roy (1993) point out that taking vertical to horizontal magnetic field ratios avoids distortion by temporal and spatial variations of the primary field. Using full tipper vectors as input data instead of directly measured magnetic field vectors also means that the amplitude and direction of the source field do not have to be known and source field variations do not affect the calculations to follow. Gharibi and Pedersen (1999) have found a procedure to extract the anomalous magnetic fields from the tipper vector using the potential field properties of the magnetic field in the air half-space. In this way, they synthesize simultaneous magnetic field measurements, which are required to solve Faraday's law (1) for the electric field. Integration of equation (1) yields only the spatial variations of the electric field. The integration constant depends on the normal conductivity distribution and must be given by appropriate boundary conditions. However, the approach of Gharibi and Pedersen (1999) is restricted

Manuscript received by the Editor May 14, 2001; revised manuscript received August 22, 2002.
*Technical University of Berlin, Institute of Applied Geosciences, Ackerstrasse 71-76, 13355 Berlin, Germany. E-mail: becken@geophysik.tu-berlin.de.
‡Uppsala University, Department of Geophysics, Villavaegen 16, 75236 Uppsala, Sweden. E-mail: lbp@geofys.uu.se.

to 2D conductivity structures, and their final solution yields only the impedance element for E-polarization (electric field is polarized parallel to the strike direction).

This paper is an extension of the work done by Gharibi and Pedersen (1999). The generalization to an arbitrary 3D conductivity distribution, presented here, is relatively straightforward, but the results can only be understood in terms of bimodal induction. Since the simplified case of E-polarization may not be used here, we will briefly describe the decomposition of currents in the earth into their toroidal and poloidal parts and discuss its consequences on the application of the transformation scheme for 3D data. Our result describes the part of the impedance tensor that is related to toroidal currents and simplifies to E-polarization in the 2D case (Weidelt, 1975). The method has been tested on synthetic noise-free data obtained with a 3D magnetotelluric modeling program. Its application to field data from an airborne survey in Sweden shows remarkable agreement with the known geology, and maps of apparent resitivities and phases illustrate the applicability of this method.

THEORY

We use right-handed Cartesian coordinates (x, y, z), where z is positive downward. The electric and magnetic fields are given with a time dependency $\{\mathbf{E},\ \mathbf{H}\} \sim e^{i\omega t}$, where ω is the angular frequency. The magnetic permeability is assumed to be the vacuum permeability μ_0 everywhere following, e.g., Vozoff (1991), which gives the choice of working with the magnetic field or the magnetic flux density $\mathbf{B} = \mu_0 \mathbf{H}$. The field relations in regions of constant conductivity σ are described by Ampere's and Faraday's laws,

$$\nabla \times \mathbf{H} = \mathbf{J}, \nabla \times \mathbf{E} = -i\omega\mu_0 \mathbf{H}, \tag{2}$$

respectively, where displacement currents are neglected in the quasi-static approximation and the current density is given by Ohm's law, $\mathbf{J} = \sigma \mathbf{E}$.

In most geophysical applications, the electromagnetic fields are measured either in the homogeneous air half-space with conductivity $\sigma = 0$ or at the surface $z = 0$. Besides the vertical electric field, which usually is not measured, all components of the electric field $\mathbf{E}$ and the magnetic field $\mathbf{H}$ are continuous across the surface and can be considered as being measured in the air half-space at $z = -0$. Let us first summarize the vector analytic properties of the electromagnetic fields in homogeneous regions and in the insulating air half-space in particular, which are needed in the following derivation.

Mode decomposition

The magnetic flux $\mathbf{B}$ and electric current density $\mathbf{J}$ (away from sources) are divergence free and may be decomposed into toroidal and poloidal parts (Schmucker and Weidelt, 1975; Weidelt, 1975; Vasseur and Weidelt, 1977; Berdichevsky and Zhdanov, 1984; McKirdy et al., 1985). The constitutive relations yield the corresponding decompositions for the magnetic and electric fields. We denote the fields connected to toroidal currents by subscript E and those related to poloidal currents by subscript M. Thus, the toroidal vectors $\mathbf{J}_E$, $\mathbf{E}_E$ and $\mathbf{B}_M$, $\mathbf{H}_M$ have no vertical components and are tangential to the earth's surface. They are considered as tangential-electric (TE-mode) and tangential-magnetic (TM-mode) systems following Schmucker and Weidelt (1975). The poloidal vectors $\mathbf{B}_E$, $\mathbf{H}_E$ complete the TE-mode and $\mathbf{J}_M$, $\mathbf{E}_M$ the TM-mode, respectively. In insulating media, $\mathbf{E}_M$ and $\mathbf{H}_E$ are potential fields. Thus, $\nabla \times \mathbf{E}_M = \mathbf{0}$ and Faraday's law yields $\mathbf{H}_M = \mathbf{0}$ here. This has the consequence that an inductively coupled source field has only a poloidal magnetic field (Berdichevsky and Zhdanov, 1984) and that poloidal currents in the earth cannot produce a toroidal magnetic field at the earth's surface. Hence, the measured magnetic field is related solely to toroidal current systems.

The terms TE- and TM-mode are obviously not standardized in geophysical literature. In magnetotellurics in particular, the TE-mode is often synonymous with E-polarization (electric field tangential to strike) and TM-mode with B-polarization (magnetic field tangential to strike). This notation is restricted to 2D conductivity structures. We use the first definition, which comprises the latter in the 2D case; e.g., $\mathbf{H}_M = \mathbf{0}$ states that no anomalous magnetic fields can be observed in B-polarization and the magnetic field is both tangential to the surface and to strike direction (see also Ward and Hohmann, 1988).

The transfer functions, which are derived from measured electromagnetic fields, may be decomposed like the fields themselves. The magnetic transfer function is entirely of TE-mode, since only poloidal magnetic fields are involved. Denoting vertical and horizontal vector components by the subscripts z and h, respectively, and the matrix transpose by the superscript T, we define the tipper vector $\mathbf{T}_E$ by the equation

$$H_{E,z} = \mathbf{T}_E^T \mathbf{H}_{E,h}. \tag{3}$$

The impedance tensor $\mathbf{Z} = \mathbf{Z}_E + \mathbf{Z}_M$ relates the horizontal poloidal magnetic field to the toroidal and poloidal horizontal electric field as

$$\mathbf{E}_{E,h} + \mathbf{E}_{M,h} = (\mathbf{Z}_E + \mathbf{Z}_M)\mathbf{H}_{E,h}. \tag{4}$$

Each element of the impedance tensor is decomposed into a transfer function of TE- and TM-mode, respectively. Note that the measured impedance is a superposition of both modes. In the following section, we develop a procedure to calculate the toroidal electric field and the related TE-mode impedance $\mathbf{Z}_E(x, y)$ from given $\mathbf{T}_E(x, y)$.

Estimation of the toroidal electric field

The subsequent derivation is more convenient in wavenumber space. The spatial Fourier transform of a function $f(\mathbf{r})$ is denoted by $\tilde{f}(\mathbf{k})$, where $\mathbf{r} = (x, y)^T$ is the horizontal space vector and $\mathbf{k} = (k_x, k_y)^T$ is the wavenumber vector. Then

$$\tilde{f}(\mathbf{k}) = \frac{1}{2\pi} \int_{-\infty}^{\infty} f(\mathbf{r}) e^{-i\mathbf{k}\cdot\mathbf{r}}\, d\mathbf{r} \tag{5}$$

and the inverse Fourier transform is given by

$$f(\mathbf{r}) = \frac{1}{2\pi} \int_{-\infty}^{\infty} \tilde{f}(\mathbf{k}) e^{i\mathbf{k}\cdot\mathbf{r}}\, d\mathbf{k}. \tag{6}$$

Derivative operators in the space domain correspond to multiplication in the wavenumber domain: $\partial/\partial x[f(\mathbf{r})]$ transforms to $ik_x \tilde{f}(\mathbf{k})$ and $\partial/\partial y[f(\mathbf{r})]$ to $ik_y \tilde{f}(\mathbf{k})$, respectively.

Since the magnetic field is a potential field in the air half-space (Rokityansky, 1982; Reitz et al. 1993), knowledge of one of its components on a (closed or infinitely extended) surface is sufficient to calculate the two remaining field components. Therefore, equation (3) can be used to uniquely determine $B_z(\mathbf{r})$ from tipper vectors $\mathbf{T}_E(\mathbf{r})$ for a given plane wave source field.

An iterative solution of the tipper decomposition is suggested similar to the one used by Gharibi and Pedersen (1999) in their 2D tipper transformation. The mathematical treatment of the 3D case is a simple expansion of the 2D solution, but calculation of the Hilbert transformation is performed in the wavenumber domain. Here, a drift in the data can easily be corrected by taking all magnetic field components to be zero at zero wavenumber.

The Hilbert transformation of a potential vector field $\mathbf{V}(\mathbf{r}, z)$, which is given on the infinitely extended plane $z = z_0$, is transformed to the wavenumber domain (Pedersen, 1989) as

$$\tilde{\mathbf{V}}_h(\mathbf{k}, z_0) = \frac{i\mathbf{k}}{k}\tilde{V}_z(\mathbf{k}, z_0), \tag{7}$$

where k denotes the absolute value of the wavenumber vector. For ease of notation, we subsequently drop the fixed variable z_0. The Hilbert transform (7) must be satisfied by the anomalous magnetic field if all field inhomogeneities are of internal origin. Taking $\mathbf{B}_h^n$ as the horizontal normal magnetic field and substituting the vertical component in expression (7) with equation (3) transformed to Fourier domain, the total horizontal magnetic field including inhomogenities attributable to conductivity anomalies in the earth is given by

$$\tilde{\mathbf{B}}_h(\mathbf{k}) = \mathbf{B}_h^n + \frac{i\mathbf{k}}{k}\left[\tilde{\mathbf{T}}^T(\mathbf{k}) * \tilde{\mathbf{B}}_h(\mathbf{k})\right], \tag{8}$$

where the asterisk denotes the convolution operator. Equation (8) is the wavenumber domain representation of a Fredholm integral equation of the second kind in the space domain. A suitable and fast method for solving such systems is the method of successive approximation, which can be performed in the wavenumber domain as follows: for a given normal magnetic field $\mathbf{B}_h^n$, a first approximation of the (anomalous) vertical field component can be estimated according to $B_z^0(\mathbf{r}) = \mathbf{T}_E^T(\mathbf{r})\mathbf{B}_h^n$. Fourier transformation to the wavenumber domain permits a first estimation of the anomalous horizontal field using equation (7). Adding the derived horizontal anomalous part to the normal field enables a new estimation of the vertical component. Hence, a number of iterations j are performed following the procedure

$$\begin{aligned} B_z^{j+1}(\mathbf{r}) &= \mathbf{T}^T(\mathbf{r})\mathbf{B}_h^j(\mathbf{r}), \\ \tilde{\mathbf{B}}_h^{a,j+1}(\mathbf{k}) &= \frac{i\mathbf{k}}{k}\tilde{B}_z^{j+1}(\mathbf{k}), \\ \mathbf{B}_h^{j+1}(\mathbf{r}) &= \mathbf{B}_h^{a,j+1}(\mathbf{r}) + \mathbf{B}_h^n. \end{aligned} \tag{9}$$

A criterion to stop the iterative process is required. Here, we use that the maximum difference of the vertical component between the present and the previous iteration $|B_z^j(\mathbf{r}_m) - B_z^{j-1}(\mathbf{r}_m)|$ at the point $(\mathbf{r}_m)$ should be less than some δB_z.

From the vertical magnetic field, we derive the toroidal electric field from Faraday's law (1). Taking $\mathbf{E}_E(\mathbf{r}) = \mathbf{E}_E^n + \mathbf{E}_E^a(\mathbf{r})$, the anomalous toroidal electric field is given in the wavenumber domain by

$$\hat{\mathbf{z}} \times \tilde{\mathbf{E}}_E^a(\mathbf{k}) = \frac{\omega\mathbf{k}}{k^2}\tilde{B}_z(\mathbf{k}), \tag{10}$$

where the vanishing horizontal divergence

$$i\mathbf{k} \cdot \tilde{\mathbf{E}}_E^a(\mathbf{k}) = 0 \tag{11}$$

is applied (the toridal electric field has no vertical component). Division by k^2 is required in equation (10), which causes numerical instability at $\mathbf{k} = \mathbf{0}$. The Fourier coefficient at this point in the wavenumber domain is equivalent to a shift in the space domain by the average anomalous field without affecting the change of the electric field. Therefore, we take $\tilde{\mathbf{E}}_E^a(\mathbf{k} = \mathbf{0}) \equiv 0$ for the moment.

Back-transformation to the space domain yields the anomalous toroidal electric field, including an unknown shift $d\mathbf{E}_E$. The total toroidal electric field is then given by $\mathbf{E}_E(\mathbf{r}) = \mathbf{E}_E^n + [\mathbf{E}_E^a(\mathbf{r}) - d\mathbf{E}_E] + d\mathbf{E}_E$. Suppose now that the impedance at one point is known, e.g., $\mathbf{Z}(\mathbf{r}_0)$, and that this measurement has been carried out in a 1D region sufficiently far away from distorting conductors. In this case, $\mathbf{E}_E^a(\mathbf{r}_0) = \mathbf{0}$; the total electric field corresponds to the normal toroidal electric field since there are no poloidal currents excited in normal regions. Furthermore, there is no magnetic anomaly to be observed. Hence, the impedance is simplified to $Z_{ij}(\mathbf{r}_0) = E_{i,E}^n / B_{j,E}^n$, from which the electric field can be calculated for any normal magnetic field. The previously estimated anomalous electric field $[\mathbf{E}_E^a(\mathbf{r}) - d\mathbf{E}_E]$ may now be shifted to the desired level at the point $(\mathbf{r}_0)$, which should result in the correct level for the whole surface, provided data were error free. Therefore, $d\mathbf{E}_E$ can be estimated from ground measurements, at least theoretically. Since the measured tipper vector is erroneous, one may expect a slight misfit of the calculated electric field. But as we shall see later, the method seems to work in a stable way and gives good structural resolution.

To describe the full three-dimensionality of the problem, the same procedure must be repeated for another primary magnetic field which is preferably polarized perpendicular to the first one. Having found horizontal electric and magnetic fields for two polarizations, we calculate the corresponding impedance tensor $\mathbf{Z}_E$ in equation (4) following, e.g., Zonge and Hughes (1991).

TE-impedance tensor and related apparent resistivity and phase

We have developed the transformation scheme to construct images of the conductivity distribution, which provide a better structural insight into the earth than magnetic transfer functions. Here, we define apparent resistivities and phases solely based on the TE-mode impedance tensor $\mathbf{Z}_E$ according to Cagniard (1953) as

$$\begin{aligned} \rho_{E,ij} &= \frac{1}{\omega\mu_0}|Z_{E,ij}|^2 \\ \phi_{E,ij} &= \arg\{Z_{E,ij}\}. \end{aligned} \tag{12}$$

Only in 1D and strictly 2D environments can the TE-impedance be related to apparent resitivities and phases one would actually measure. However, in realistic (3D) geological situations, the modes are coupled inside the earth, and

the measured impedance tensor cannot be rotated to decouple into E- and B-polarization with vanishing main-diagonal elements. Thus, only in the 2D case will the transformation scheme yield exact E-polarization apparent resistivities and phases, provided a normal impedance Z_n is known. Thus, for a structure striking in the x-direction,

$$\mathbf{Z}_E = \begin{pmatrix} 0 & Z_n + Z^a_{E,xy} \\ -Z_n & 0 \end{pmatrix}. \tag{13}$$

In general, the anomalous part of the impedance is distributed over all elements of the tensor. Thus, a rotational invariant is more suitable for visualizing the structures. For this purpose, the determinant $\|\mathbf{Z}_E\|$ is calculated according to

$$\|\mathbf{Z}_E\| = Z_{E,xx}Z_{E,yy} - Z_{E,xy}Z_{E,yx}. \tag{14}$$

However, using equation (14), anomalies are always underestimated. Consider, for instance, a 2D structure: taking the determinant of equation (13) is actually the geometric mean of the E-polarization and the normal impedance, respectively. Thus, apparent resitivities are biased by the normal structure, though the structure itself remains resolved.

A peculiarity in defining the normal structure can be noticed. Consider, for instance, two quarter-spaces, which is a transition anomaly. Sufficiently far away from the contact, both media may be considered as one dimensional; thus, only toroidal electric fields exist. To explain the normal electric field on an arbitrarily chosen side of the contact, a normal toroidal electric field is sufficient; but on the opposite side, a spatially constant poloidal electric field is required which, when added to the normal toroidal electric field, gives the correct total electric field. Usually we consider TM-mode fields as anomalous, which implies spatial nonuniformity. Thus, the determinant on the opposite side underestimates the anomaly because the constant poloidal fields cannot be taken into account.

An alternative rotational invariant of the impedance tensor can be used to overcome this problem. From equations (13) and (14), we can express the E-polarization impedance $Z_{E,2d} = Z_n + Z^a_{E,xy}$ independent of the measurement coordinate system according to

$$Z_{E,2d} = -\frac{\|\mathbf{Z}_E\|}{Z_n}, \tag{15}$$

since only rotational invariants are involved. The negative sign produces phases in the first quadrant, provided Z_n is defined with phase in the third quadrant. For 3D impedances, equation (15), which is a simple manipulation of the determinant, can be used as an optimal approximation to E-polarization. Note that $Z_{E,2d}$ can be obtained without the critical step of determining rotation angle.

A SYNTHETIC EXAMPLE

A powerful 3D modeling code (Avdeev et al., 2002) has been used to generate synthetic data for testing the transformation algorithm. Electromagnetic fields are calculated by the integral equation technique, combining Krylov subspace iteration with the modified iterative dissipative method.

The model, sketched in Figure 1, consists of two inhomogeneous layers, embedded in a normal background structure of 1000 Ω m for the upper 60 m and 10 000 Ω m below. Both layers have a thickness of 10 m and are at 0–10 m and 50–60 m depth. The top layer contains a figure eight-shaped 3D structure of 100 Ω m; the second layer describes an elongated conductor of 2 Ω m. This model shall simulate a typical situation of shallow structures in Sweden: the loops in the surface layer sketch alluvial fillings of minor valleys around basement outcrops, while the deeper conductor simulates a thin mineralized zone—all embedded in resistive crystalline rocks forming the background structure. The frequency used for forward modeling is 16 kHz.

The total model area (1100 × 1350 m) for numerical calculations exceeds the area shown in Figures 1–3 (500 × 750 m) by a frame of 300 m. The enlarged model guarantees the 2D character of the deep, elongated conductor. Quadratic model cells with a base length of 5 m result in a horizontal discretization of 220 × 270 model cells. The vertical discretization of both inhomogeneous layers varies between 2 and 5 m.

The transformation algorithm has been applied to the modeled magnetic transfer functions shown as Wiese induction arrows (Parkinson, 1959; Schmucker, 1970) in Figures 2a and 2b, respectively. Since the data are discrete and the area of investigation is bounded, we have to impose boundary conditions to be satisfied in a practical implementation. The Fourier analysis of discretely sampled functions is based on the assumption of a periodic continuation of the function in space domain. Thus, 2D features extending over the whole area as in the deeper layer are permitted. However, to avoid Gibb's oscillations, a taper window is applied prior to Fourier transformation, suppressing all anomalies at the model borders.

The normal structure is known in this case, and knowledge of the medium electric field was obtained from comparison with the measured impedance in the northwestern model corner. A small bias was introduced because here the anomalous fields are not exactly zero and in particular the elongated conductor is still visible at the upper model border. Thus, we may expect a slight misfit of apparent resistivities, as we always expect on field data.

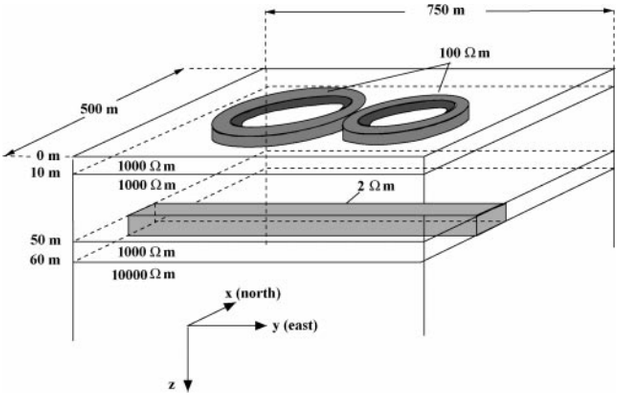

FIG. 1. Sketch of model. The surface layer with a thickness of 10 m contains a double-loop structure of 100 Ω m, representing sediment-filled valleys. An elongated conductor with 2 Ω m in a depth from 50–60 m indicates a fractured zone. Inhomogeneities are embedded in a background normal structure of 1000 Ω m in the upper 60 m and 10 000 Ω m below. The model simulates typical 3D conductivity distributions in basement-dominated areas of Sweden.

Let us first consider a profile $\overline{AB}$ across the model at position east = 245 m passing the center of the western loop perpendicular to the deep conductor. This profile is approximately two dimensional. In Figures 2c and 2d we compare true apparent resistivities and phases from forward modeling (Z_{xy} corresponds to B-polarization in a 2D approximation, Z_{yx} to E-polarization, respectively) with the result of the transformation $Z_{E,xy}$ and $Z_{E,yx}$ and in Figures 2e and 2f with the invariant representations $\|\mathbf{Z}_E\|$ and $Z_{E,2d}$.

Real and imaginary induction arrows (Figures 2a and 2b) and true apparent resitivities and phases (solid and dash-dotted lines in Figures 2c–2f) clearly indicate the upper and lower inhomogenities, respectively, at 16 kHz frequency. Note that real induction arrows mainly point away from the shallow loop conductor, whereas imaginary induction arrows point toward the elongated conductor in the lower inhomogeneous layer. The value Z_{xy} is strongly distorted by charge accumulation at the loop boundaries, giving rise to poloidal currents. There is almost no anomalous field to be observed in the corresponding TE-impedance element $Z_{E,xy}$ (closed circles in Figures 2c and 2d), since the profile is approximately in a 2D environment. On the other hand, the impedance $Z_{E,yx}$ (open circles) shows a similar characteristic as Z_{yx} in both apparent resistivity and phase, but the apparent resistivity cannot be recovered exactly.

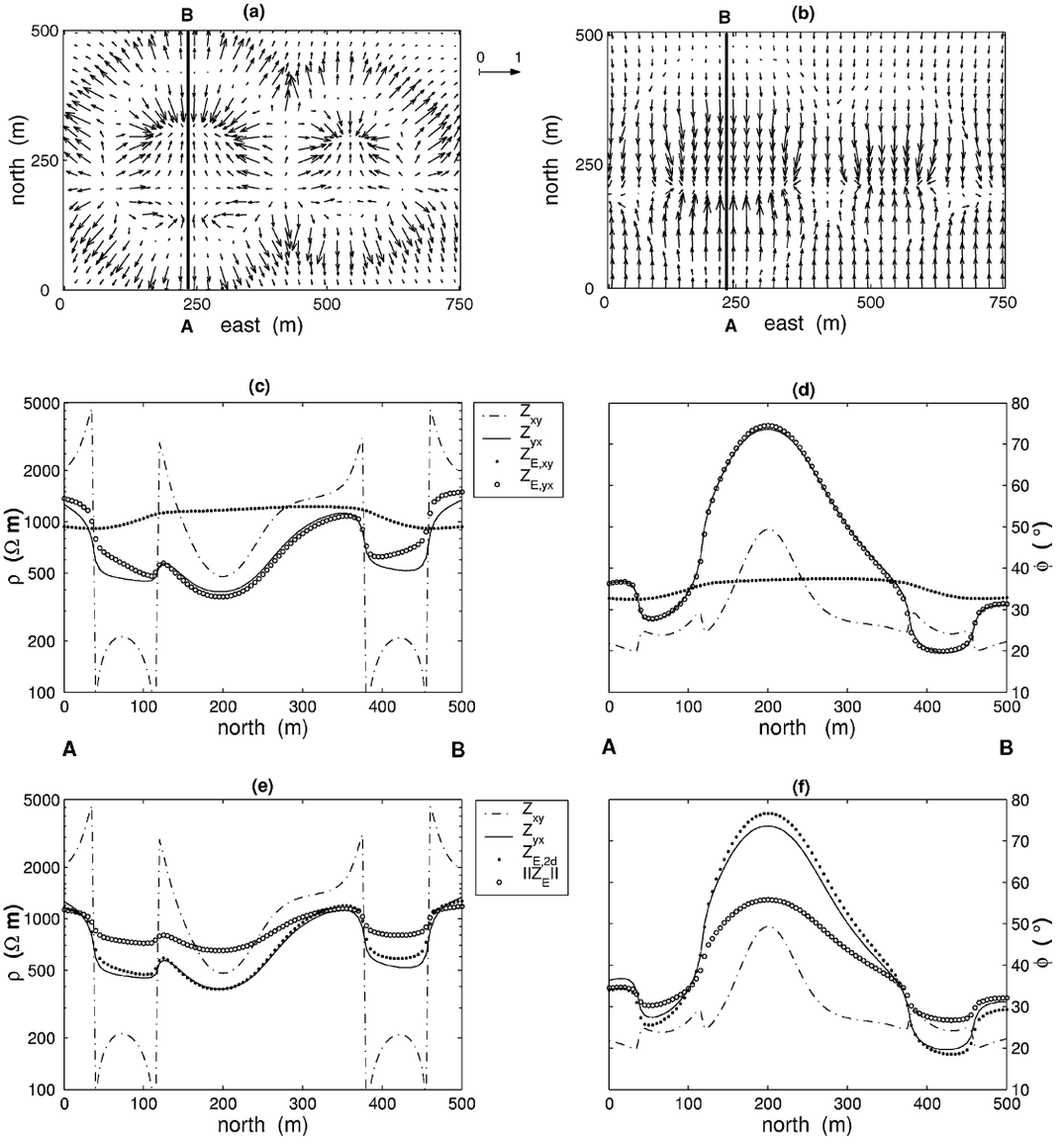

FIG. 2. Model calculations. (a) Real and (b) imaginary Wiese induction arrows representing modeled magnetic transfer functions. Only every fifth point is plotted. (c) Apparent resitivity and (d) phase along profile $\overline{AB}$ indicated in maps of induction arrows. Solid and dash-dotted lines denote modeled impedance elements Z_{yx} and Z_{xy}, respectively. Open and closed circles indicate off-diagonal elements $Z_{E,yx}$ and $Z_{E,xy}$ of TE-mode impedance tensor, respectively. (e), (f) Modeled impedances (Z_{yx}—solid line; Z_{xy}—dash-dotted line) are compared to the invariant representations $Z_{E,2d}$ (closed circles) and $\|Z_E\|$ (open circles).

Thus, in this particular model at the frequency used for model calculations, phases are less distorted by poloidal currents than apparent resistivities are. In other words, phases look deeper to the 2D conductor and exhibit a 2D character.

Using the invariant representations (14) and (15), respectively, shown in Figures 2e and 2f, the shape of Z_{yx} can be recovered in both apparent resistivities and phases. The determinant (open circles) reveals the structures with fewer side effects in the apparent resitivity than $Z_{E,yx}$, but the anomalies are underestimated as expected. The optimal E-polarization approximation $Z_{E,2d}$ yields acceptable values of apparent resistivities and phases compared to Z_{yx}, although the fit of the phase on this particular profile is worse than $Z_{E,yx}$.

Figures 3a–3d show maps of apparent resitivies and phases for the whole model area. White and light gray denote low and dark gray and black indicate high apparent resistivities and phases, respectively. True apparent resitivities (Figures 3a and 3b) related to the impedance element Z_{yx} image the loop conductor, while phases indicate both the loop and the deep conductor beneath. Apparent resistivities show the discontinuous behavior of the electric field with a component perpendicular to the loop conductor pronouncing the boundary of the loops. Thus, white in Figure 3a is from the poloidal electric field and cannot be seen in the TE-mode invariant $Z_{E,2d}$ in Figure 3c. Still, the loop conductor is easily identified in Figure 3c, and in some sense it is less distorted by 3D effects than in Figure 3a. Phases of Z_{yx} and $Z_{E,2d}$ in Figures 3b and 3d, respectively, clearly indicate the existence and location of the deeper conductor in a similar way, while the surface loop is still visible.

Obviously, apparent resistivies and phases of the invariant representation (15) of the TE-mode impedance tensor are reasonable indicators of the electrical conductivity distribution in the subsurface even in complex 3D cases as used for this model study.

APPLICATION TO AIRBORNE VLF DATA IN SOUTHEASTERN SWEDEN

This description of an application to field data demonstrates that the suggested algorithm is stable, yields reasonable results, and facilitates interpretation of magnetic transfer functions in VLF applications. We have chosen field data from an area where the geology is known and the results can easily be checked for their plausibility.

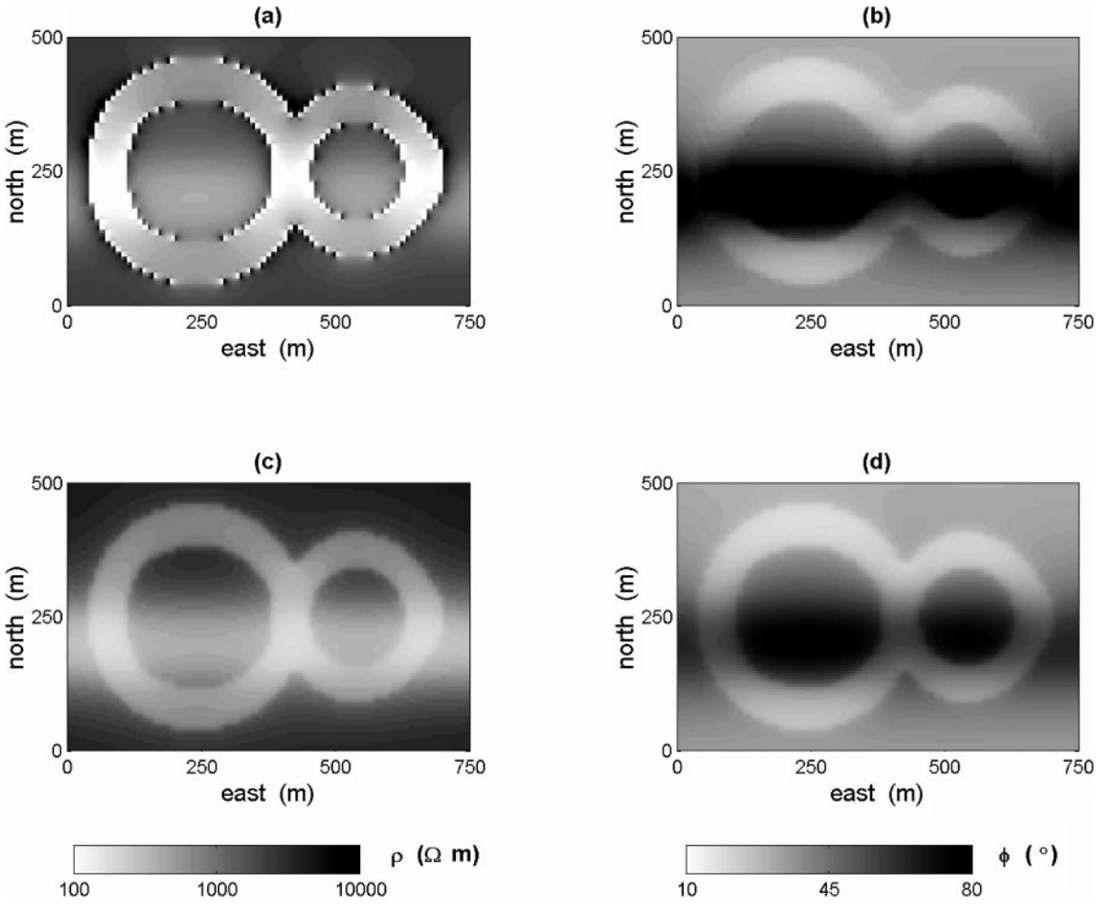

FIG. 3. Model calculations. (a) Apparent resistvity and (b) phase related to Z_{yx} from forward modeling. (c) Apparent resistivity and (d) phase estimated from magnetic transfer functions shown in terms of the invariant $Z_{E,2d}$. Differences in the maps, which are significant in the apparent resistivities, occur because of poloidal currents, which do not affect the calculated TE-mode impedance tensor and its invariants. The phase of Z_{yx} is less distorted by 3D effects because of charge accumulation, resulting in a great semblance to the phase of $Z_{E,2d}$.

The data shown here were collected and provided by the Geological Survey of Sweden (SGU) during airborne surveys in Sweden. They used the Rugby (United Kingdom) and Bordeaux (France) transmitters to estimate magnetic transfer functions for frequencies around 16 kHz. Their azimuthal angles differ by about 20°. Fortunately, the predominant strike direction in the measurement area is east-west. Northward-striking structures are poorly resolved because of the choice of transmitters.

For the purpose of the 3D tipper transformation, the original irregularly spaced data (flight line separation ~200 m, lines in south–north direction, point distance on each line ~15–20 m) were interpolated to a regular grid of 50 m point-to-point distance in both north and east directions. We did not perform a downward continuation of the fields from the measurement height (~70 m) to the surface, since this would create some instability from noise in the data. The data were manipulated with a taper window, which is equal to one everywhere except on the borders, where it smoothly decays to zero. The decay area was restricted to a small part of the whole area under consideration. Tipper data were then decomposed using equation (10), where a maximum difference criterion of 0.001% with respect to the normal field was used. Convergence problems may occur in the case of heavily distorted data which are not of internal origin. Such areas should be excluded from a transformation, e.g., by tapering the tipper vector in those areas to zero. In the present case, all data could be used and convergence was reached after around 50 iterations for each primary field polarization.

Geological background

The area investigated lies within the map Stockholm 10 I SO (SGU), southeast of Stockholm, and is part of the Bergslagen region, which has been a major metal producer for more than a millennium (Allen et al., 1996). The Bergslagen area is the type location of the term *skarn* and several other mineral species. Banded iron formations and various types of skarn deposits build a diverse range of ore deposits. Most of them occur in metavolcanic rocks and associated facies. Figure 4a shows a simplified geological map of the bedrock. The basement, covered to a great extent by quaternary sediments, is of early Proterozoic age and part of a felsic magmatic region of mainly medium to high metamorphic grade in the Baltic shield. Allen et al. (1996) interpret the region as an extensional basin in the environment of an active continental margin, comprising several stages of pre- and posttectonic magmatic intrusions through the evolution.

The metavolcanic (yellow and light green) and metasedimentary (blue) rocks shown are deformed into steep, doubly plunging, mainly east–west-oriented synclines, partly wrapping around rheologically more competent granitoid and granodioritic intrusions (brown). Thin, sheet-like intrusions were involved in the folding and show up as macrofolds of wavelengths of >30 km (Stalhos, 1981) embedded in deformed metasediments.

Since the competent rocks were resistant to glacial erosion during the Quaternary ice-sheet coverage of the Baltic shield, they gently build up as topographic highs. The valleys, covered by thin electrical conductive Quaternary alluvium, indicate underlaying rheologically weaker metavolcanics and metasediments.

Maps of apparent resistivities and phases

As an example of the data set, the real part of T_x is shown in Figure 4b, mainly indicating east–west-striking structures. The 15×25 km area is the same as shown in the geological map (Figure 4a). Typical values of the tipper in this area range from -0.5 to 0.5. The plot is superimposed by the topography, which is plotted as a gray-shaded relief.

In the absence of ground impedance measurements, the required mean electric field over the whole area was estimated by assuming a homogeneous earth with a resistivity of 2000 Ωm, representing the crystalline basement rocks described previously. It should be taken into account that the range of apparent resistivities and phases is thereby determined. Hence, one should focus on their lateral changes rather than on their absolute values.

Figures 4c and 4d show the results of the tipper transformation in terms of apparent resistivity and phase using the invariant representation of equation (15), superimposed by the topography as a gray-shaded relief. Blue denotes high apparent resistivities and phases below 45°, whereas red indicates low apparent resistivities and high phases, respectively. White lines mark the coastline and lakes.

Apparent resistivity and phase correlate significantly with lithological units, as shown in the geological map. The apparent resistivity is low in sediment-filled valleys, described previously, whereas the phase is higher than 45° in these regions, indicating deep conductors, e.g., in the form of highly mineralized metasediments and metavolcanics (Allen et al., 1996). The massive granitoid blocks shown in the geological map clearly appear as electrically highly resistive structures. Here, the phase is lower than 45°, indicating an increasing resistivity with depth. This coincides with a simplified depth sequence of a thin layer of conductive overburden and an underlying, highly resistive (but weathered in the near surface) crystalline rock.

Fault zones are marked by low resistivities (if they are fluid filled) and build a pattern of south–southeast- and east–northeast-striking features. Many details given in the geological map can be recovered from the map of apparent resistivities, and vice-versa, but this is not described further here.

The results are very satisfactory and are easily interpreted. Improvements could be achieved by using two transmitters perpendicular to each other to enhance the resolution of north-striking features and by using more frequencies to improve depth resolution. Furthermore, involving ground measurements to obtain information about the normal structure can help to eliminate the uncertainties introduced into the maps by simply assuming a medium electric field as was done in this example.

CONCLUSION

The transformation of magnetic transfer functions into apparent resistivities and phases is a new representation of VLF data. Interpretation of magnetic transfer functions is rather difficult because they mainly indicate lateral changes of the earth's conductivity distribution. Information about the depth dependency of the structures is given in terms of the mutual sign relation between the real and imaginary parts of the transfer functions, i.e., their phases. Extracting this information cannot be obtained by visually analyzing the maps. The new

representation in terms of apparent resistivity and phases clearly indicates lithological units in complicated 3D geological environments and gives an idea about the depth profile by interpreting phases.

The apparent resistivities and phases are calculated iteratively, exploiting the potential field character of the magnetic field in the air and the vector analytic properties of the electric field formally introduced by the decomposition into its toroidal and poloidal parts. Only a simple mathematical tool is required to estimate the toroidal electric field besides a constant. The unknown constant has to be estimated by other means—for instance, by an impedance ground measurement. From the

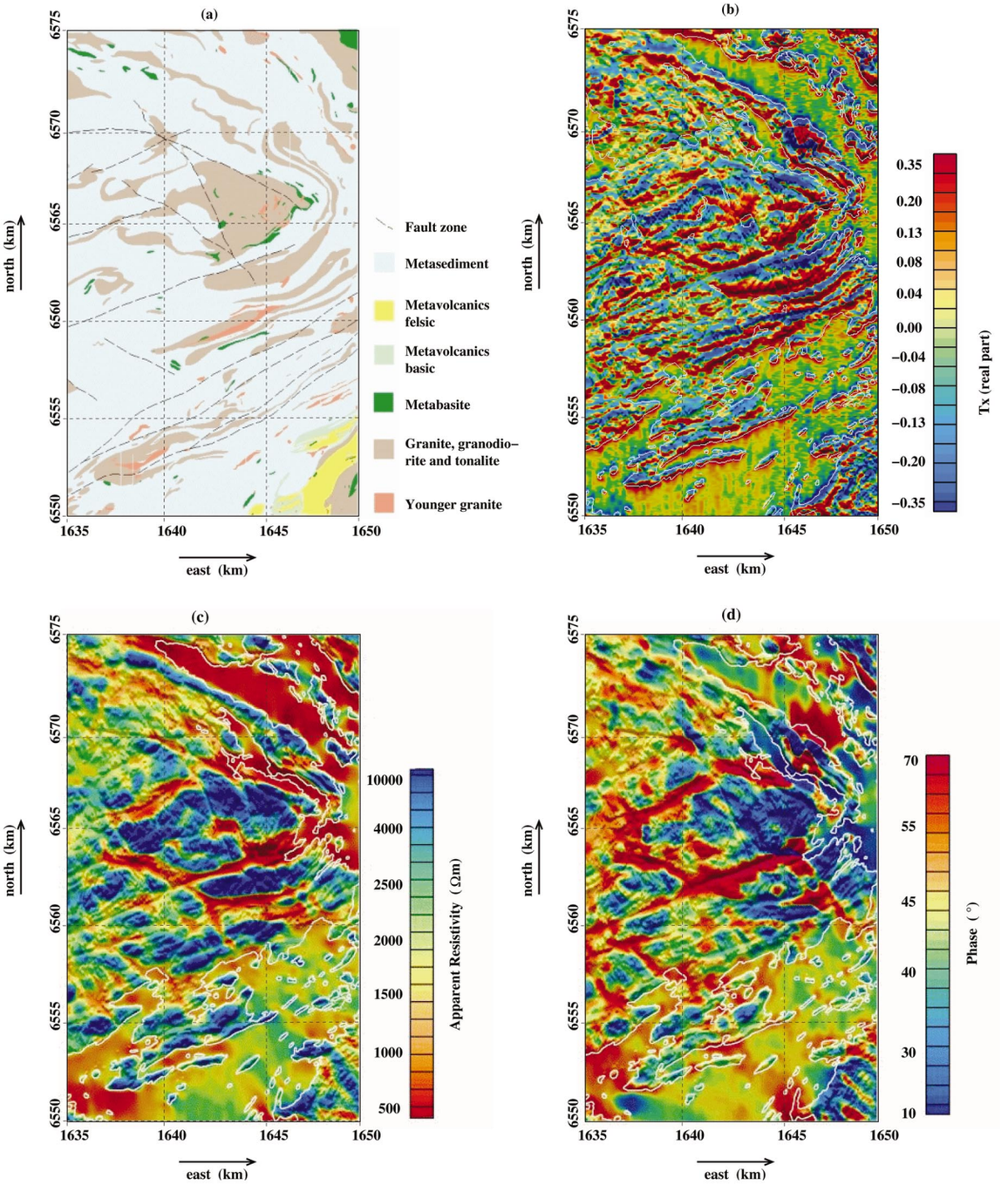

FIG. 4. Airborne VLF measurements from Sweden. (a) Geological map of the area of investigation (Bergslagen region, southeastern Sweden). (b) Real part of one component of the measured tipper (T_x). (c) Invariant representation $Z_{E,2d}$ of the TE-mode impedance tensor in terms of apparent resistivity and (d) phase estimated by the transformation of tipper data. See text for description. Maps are reprinted with permission of the SGU.

magnetic and toroidal electric fields for two independent primary field polarizations, we calculate an impedance tensor representing the TE-mode response of a 3D earth. When boundary information about the normal structure is not available, we can still obtain reasonable impedances, although the level of apparent resitivity and phase is biased. However, this does not degrade the significant correlation of the maps of invariant representations of the impedance tensor with the known geology.

ACKNOWLEDGMENTS

The Geological Survey of Sweden (SGU) generously put their geological and geophysical maps at our disposal. Martin Engels kindly calculated the synthetic 3D responses used to illustrate the method.

REFERENCES

Allen, R. L., Lundstroem, I., Ripa, M., Simeonov, A., and Christofferson, H., 1996, Facies analysis of a 1.9 ga continental margin, back-arc, felsic caldera province with diverse Zn-Pb-Ag-(Cu-Au) sulfide and Fe oxide deposits, Bergslagen region, Sweden: Econ. Geol., **91**, 979–1008.

Avdeev, D. B., Kuvshinov, A. V., Pankratov, O. V., and Newman, G. A., 2002, Three-dimensional induction logging problems, part I: An integral equation solution and model comparison: Geophysics, **67**, 413–426.

Berdichevsky, M. N., and Zhdanov, M. S., 1984, Advanced theory of deep geomagnetic sounding: Elsevier Science Publ. Co., Inc.

Cagniard, L., 1953, Basic theory of the magneto-telluric method of geophysical prospecting: Geophysics, **18**, 605–635.

Gharibi, M., and Pedersen, L. B., 1999, Transformation of VLF data into apparent resistivities and phases: Geophysics, **64**, 1393–1402.

McKirdy, D. M., Weaver, J. T., and Dawson, T. W., 1985, Induction in a thin sheet of variable conductance at the surface of a stratified earth–II: Three-dimensional theory: Geophys. J. Roy. Astr. Soc., **80**, 177–194.

Parkinson, W. D., 1959, Direction of rapid geomagnetic fluctuations: Geophys. J., **2**, 1–14.

Pedersen, L. B., 1989, Relations between horizontal and vertical gradients of potential fields (short note): Geophysics, **54**, 662–663.

Pedersen, L. B., Qian, W., Dynesius, L., and Zhang, P., 1994, An airborne tensor VLF system, from concept to realization: Geophys. Prosp., **42**, 863–883.

Reitz, J., Milford, F., and Christy, R., 1993, Foundations of electromagnetic theory: Addison-Wesley Publ. Co.

Rokityanski, I. I., 1982, Geoelectric investigation of the Earth's crust and mantle: Springer Pub. Co., Inc.

Roy, J., 1993, Discussion on "Effect of temporal and spatial variations of the primary signal on VLF total-field surveys," by M. A. Vallee, M. Chouteau, and G. J. Palacky with replies by authors: Geophysics, **58**, 756–757.

Schmucker, U., 1970, An introduction to induction anomalies: J. Geomagn. Geoelectr., **22**, 9–33.

Schmucker, U., and Weidelt, P., 1975, Electromagnetic induction in the earth: Lectures notes, Aarhus Univ.

Stalhos, G., 1981, A tectonic model for the Svecokarelian folding in east central Sweden: GFF (Geologiska Foreningens i Stockhom Forhandlingar), **103**, 33–46.

Vallee, M. A., Chouteau, M., and Palacky, G. J., 1992, Effect of temporal and spatial variations of the primary signal on VLF total-field surveys: Geophysics, **57**, 97–105.

Vasseur, G., and Weidelt, P., 1977, Bimodal electromagnetic induction in non-uniform thin-sheets with an application to the northern Pyrenan anomaly: Geophys. J. Roy. Astr. Soc., **51**, 669–690.

Vozoff, K., 1991, The magnetotelluric method, *in* Nabighian, M. N., Ed., Electromagnetic methods in applied geophysics: Soc. Expl. Geophys., 641–711.

Ward, S. H., and Hohmann, G. W., 1988, Electromagnetic theory for geophysical applications, *in* Nabighian, M. N., Ed., Electromagnetic methods in applied geophysics: Soc. Expl. Geophys., 131–312.

Weidelt, P., 1975, Electromagnetic induction in three-dimensional structures: J. Geophys., **41**, 85–109.

Zonge, K. L., and Hughes, L. J., 1991, Controlled source audio-frequency magnetotellurics, *in* Nabighian, M. N., Ed., Electromagnetic methods in applied geophysics: Soc. Expl. Geophys., 713–809.